Science Advances
AAAS

Supplementary Materials for

On-chip generation of single-photon circularly polarized single-mode vortex beams

Xujing Liu *et al.*

Corresponding author: Sergey I. Bozhevolnyi, seib@mci.sdu.dk

Sci. Adv. **9**, eadh0725 (2023)
DOI: 10.1126/sciadv.adh0725

This PDF file includes:

Supplementary Text

Note 1: Theoretical analysis of SPP scattering into circularly polarized light

(1) Producing RCP with anisotropic nanobricks

We first introduce conventions for describing the light fields, a plane electromagnetic wave is of the form (*52*):

$$\boldsymbol{E}_{pr}\sim\boldsymbol{E}_0\exp\{i(\omega t-\boldsymbol{k}\cdot\boldsymbol{r})\}\ \rightarrow\boldsymbol{E}_{pr}\sim\boldsymbol{E}_0\exp(-i\boldsymbol{k}\cdot\boldsymbol{r}) \tag{S1}$$

where $\boldsymbol{E}_0$ is the electric field vector, ω is the angular frequency, the wave vector is, $\boldsymbol{k}=2\pi/\lambda$, λ is the wavelength of the wave. For a right-hand circularly polarized (RCP) wave travelling in the +*z* direction:

$$\boldsymbol{E}_{pr}\sim E_0\frac{1}{\sqrt{2}}\begin{pmatrix}1\\-i\end{pmatrix}\exp\{i(\omega t-\boldsymbol{k}\cdot\boldsymbol{r})\}\sim E_0\begin{pmatrix}1\\-i\end{pmatrix}\exp(-ikz) \tag{S2}$$

We consider the SPP incidence on a doublet of (extremely) anisotropic scatterers displaced by a quarter of the SPP wavelength along the propagation direction as shown in fig. S1A, considering only the in-plane (*x*, *y*) field components, the incident SPP field has only one component:

$$\boldsymbol{E}_{SPP}\sim E_0(1,\ 0)\exp(-ik_{SPP}x) \tag{S3}$$

The (largest) field component scattered by this doublet in the *z* direction can be written as follows:

$$\boldsymbol{E}_{scl}\sim C_1\begin{pmatrix}1+\exp\left(-i\frac{\pi}{2}\right)\\-1+\exp\left(-i\frac{\pi}{2}\right)\end{pmatrix}=C_1\begin{pmatrix}1-i\\-1-i\end{pmatrix}=C_1(1-i)\cdot\begin{pmatrix}1\\-i\end{pmatrix}\sim C_1\cdot e^{-i\frac{\pi}{4}}\cdot\begin{pmatrix}1\\-i\end{pmatrix} \tag{S4}$$

If we consider the contributions from the short side of a nanobrick, the scattered field component is relatively small and can then be written as follows:

$$\boldsymbol{E}_{scs}\sim C_2\begin{pmatrix}1+\exp\left(-i\frac{\pi}{2}\right)\\1-\exp\left(-i\frac{\pi}{2}\right)\end{pmatrix}=C_2\begin{pmatrix}1-i\\1+i\end{pmatrix}\sim C_2\cdot e^{-i\frac{\pi}{4}}\cdot\begin{pmatrix}1\\i\end{pmatrix} \tag{S5}$$

Conclusions:

1) The largest scattered field components produce an RCP wave travelling in the +*z* direction (i.e., towards us), while the minor scattered field components result in an LCP wave travelling in the +*z* direction ($C_1\gg C_2$).
2) The net scattering in both cases is coming from the doublet centre as reflected by the factor $e^{-i\frac{\pi}{4}}$.

(2) Producing RCP vortices

Considering the SPP field propagating under an azimuthal angle φ with the *x*-axis (fig. S1B), the largest contribution to the scattered field can be expressed as follows:

$$\boldsymbol{E}_{scl}(\varphi)\sim C_1\cdot\begin{bmatrix}\cos\varphi & -\sin\varphi\\ \sin\varphi & \cos\varphi\end{bmatrix}\cdot\begin{pmatrix}1\\-i\end{pmatrix}=C_1\begin{pmatrix}\cos\varphi+i\sin\varphi\\ \sin\varphi-i\cos\varphi\end{pmatrix}=C_1e^{i\varphi}\begin{pmatrix}1\\-i\end{pmatrix} \tag{S6}$$

Consequently, the minor contribution to the scattered field can be expressed as follows:

$$\boldsymbol{E}_{scs}(\varphi)\sim C_2\cdot\begin{bmatrix}\cos\varphi & -\sin\varphi\\ \sin\varphi & \cos\varphi\end{bmatrix}\cdot\begin{pmatrix}1\\i\end{pmatrix}=C_2\begin{pmatrix}\cos\varphi-i\sin\varphi\\ \sin\varphi+i\cos\varphi\end{pmatrix}=C_2e^{-i\varphi}\begin{pmatrix}1\\i\end{pmatrix} \tag{S7}$$

Conclusions:

1) The largest scattered field components originating from concentric circles of doublets (separated by the SPP wavelength) produce an RCP vortex field with the +1 topological

charge travelling in the $+z$ direction (i.e., towards us), while the minor scattered field components result in an LCP vortex field with the -1 topological charge.

2) Considering the largest scattered field components producing RCP fields, in order to produce an RCP wave (without topological charges) one should have a diverging (from the centre) spiral of nano-bricks with the distance from the centre (QE) increasing with the angle φ:

$$\varphi = k_{SPP} \cdot \delta r(\varphi) \rightarrow r(\varphi) = r_0 + \frac{\varphi}{k_{SPP}} \tag{S8}$$

In order to add the compensating phase:

$$\boldsymbol{E}_{SPP}(\varphi) \sim E_0 \begin{pmatrix} \cos\varphi \\ \sin\varphi \end{pmatrix} \exp(-ik_{SPP}r) \sim \exp(-i\varphi) \tag{S9}$$

3) Using converging (towards the centre) spiral would result in an RCP vortex field with the +2 topological charge travelling in the $+z$ direction.

4) In order to produce an RCP vortex with the -1 topological charge, one should use a twice fast diverging spiral:

$$2\varphi = k_{SPP} \cdot \delta r(\varphi) \rightarrow r(\varphi) = r_0 + \frac{2\varphi}{k_{SPP}} \tag{S10}$$

The compensating phase is:

$$\boldsymbol{E}_{SPP}(\varphi) \sim E_0 \begin{pmatrix} \cos\varphi \\ \sin\varphi \end{pmatrix} \exp(-ik_{SPP}r) \sim \exp(-i2\varphi) \tag{S11}$$

(3) Producing LCP with anisotropic nanobricks

We consider then the SPP incidence on a mirrored doublet of (extremely) anisotropic scatterers displaced by a quarter of the SPP wavelength along the propagation direction as shown in fig. S1C: The (largest) field scattered by this doublet in the z direction can be written as follows:

$$\boldsymbol{E}_{scl} \sim C_1 \left(1 + exp\left(-i\frac{\pi}{2}\right), -1 + exp\left(-i\frac{\pi}{2}\right)\right) = C_1 \begin{pmatrix} 1-i \\ -1-i \end{pmatrix}$$

$$= C_1(1-i) \cdot \begin{pmatrix} 1 \\ \frac{-1-i}{1-i} \end{pmatrix} = C_1(1-i) \cdot \begin{pmatrix} 1 \\ -i \end{pmatrix} \sim C_1 \cdot e^{-i\frac{\pi}{4}} \cdot \begin{pmatrix} 1 \\ -i \end{pmatrix} \tag{S12}$$

If we consider the contributions from the short side of a nanobrick, the scattered field can then be written as follows:

$$\boldsymbol{E}_{scs} \sim C_2 \left(1 + \exp\left(-i\frac{\pi}{2}\right), -1 + \exp\left(-i\frac{\pi}{2}\right)\right) = C_2 \begin{pmatrix} 1-i \\ -1-i \end{pmatrix} \sim C_2 \cdot e^{-i\frac{\pi}{4}} \cdot \begin{pmatrix} 1 \\ -i \end{pmatrix} \tag{S13}$$

(4) Producing LCP vortices

Considering the SPP field propagating under the angle φ with the x-axis as shown in fig. S1D, the largest contribution to the scattered field can be expressed as follows:

$$\boldsymbol{E}_{scl}(\varphi) \sim C_1 \cdot \begin{bmatrix} \cos\varphi & -\sin\varphi \\ \sin\varphi & \cos\varphi \end{bmatrix} \cdot \begin{pmatrix} 1 \\ i \end{pmatrix} = C_1 \begin{pmatrix} \cos\varphi - i\sin\varphi \\ \sin\varphi + i\cos\varphi \end{pmatrix} = C_1 e^{-i\varphi} \begin{pmatrix} 1 \\ i \end{pmatrix} \tag{S14}$$

Consequently, the minor contribution to the scattered field can be expressed as follows:

$$\boldsymbol{E}_{scs}(\varphi) \sim C_2 \cdot \begin{bmatrix} \cos\varphi & -\sin\varphi \\ \sin\varphi & \cos\varphi \end{bmatrix} \cdot \begin{pmatrix} 1 \\ -i \end{pmatrix} = C_2 \begin{pmatrix} \cos\varphi + i\sin\varphi \\ \sin\varphi - i\cos\varphi \end{pmatrix} = C_2 e^{i\varphi} \begin{pmatrix} 1 \\ -i \end{pmatrix} \tag{S15}$$

Conclusions:

1) The largest scattered field components originating from concentric circles of doublets (separated by the SPP wavelength) produce an LCP vortex field with the -1 topological charge travelling in the $+z$ direction, while the minor scattered field components result in an RCP vortex field with the +1 topological charge.

2) Considering the largest scattered field components producing LCP fields, in order to produce an LCP wave (without topological charges) one should have a converging (to the centre) spiral of nano-bricks with the distance from the centre (QE) decreasing with the angle φ:

$$\varphi = -k_{SPP} \cdot \delta r(\varphi) \rightarrow r(\varphi) = r_0 - \frac{\varphi}{k_{SPP}} \quad \text{(S16)}$$

In order to add the compensating phase:

$$\boldsymbol{E}_{SPP}(\varphi) \sim E_0(\cos\varphi, \sin\varphi) \exp(-ik_{SPP}r) \sim \exp(i\varphi) \quad \text{(S17)}$$

3) Using diverging (from the centre) spiral would result in an LCP vortex field with the -2 topological charge travelling in the $+z$ direction (with the strategy for producing positive topological charges being reversed).

(5) Concluding remarks

The ratio between the strongest and weakest scattered field components is determined by the length-to-width ratio of nanorods (nanobricks or anisotropic scatterers) but is not directly proportional to that. The corresponding dependence is influenced by the nanobrick shape and includes the nanobrick height and the refractive index as well. Nanofabrication along with the design principle limits the largest length-to-width ratio that can realistically be fabricated. For example, it is often very difficult to fabricate a nanobrick with the width smaller than the height. Given the nanobrick separation equal to a quarter of the SPP wavelength implies that the nanobrick length is limited to $\sqrt{2}\lambda_{SPP}/4$ to avoid the overlap of two orthogonal nanobricks (fig. S1). Finally, the scattering strength should not be too small for the out-of-plane SPP scattering being stronger than the SPP absorption, and that requires to fabricate nanobricks with sufficiently large volumes, i.e., with sufficiently large heights. It is then clear that the overall optimization would require to use nanobrick materials with larger refractive indexes, relaxing thereby the requirements of large volumes (the scattering strength increases with the refractive index contrast). Our choice of the nanobrick parameters [Fig. 1B in the main text] is a result of numerical optimization involving extensive simulations and backed up with the control experiments.

Note 2. Experiment of SPP scattering into circularly polarized light

With the numerical simulations showing that the surface plasmon polaritons could be efficiently outcoupled to free-space circular polarized light by the designed anisotropic element, here, we conducted experimental characterization to investigate the performance of anisotropic units, which is the elementary component for the SPP coupler (metasurface B shown in Fig. 3(a)). The excitation of propagating SPPs is realized by a grating A (HSQ) on SiO_2 (20 nm) /Ag (150 nm) substrate. The period is 580 nm with the width of 140 nm, enabling the excitation of SPP with 670 nm laser light. The distance between grating A and metasurface B is 10 μm, considering the trade-off between the overlap of incident beam and outcoupling light and the SPP loss along propagation. A wavelength-tuneable continuous-wave laser (NKT, SuperK EXTREME/FIANIUM) is used as the incident light after converting to TM wave with a polarizer, then focused on the centre of the grating A. As clearly shown in Fig. 3(b), SPP can be excited and then coupling out by metasurface B, confirming its ability for acting as an efficient SPP outcoupler. To characterize the polarized states, a quarter wave plate and linear polarizer is inserted before the CMOS camera to measure the Stokes parameter S_3 (shown in the Fig. 3(c)). Fig. 3(d) shows the 2D distribution of S_3. Reflected light of grating A keeps the linear polarization, while the

outcoupling emission from metasurface B is circular polarized with S_3 = 0.98. It proves that the SPPs can be efficiently outcoupled to free-space circular polarized light by the designed anisotropic element.

Note 3. Polarization measurement

The Stokes polarization parameters are directly measurable based on intensity quantities. The emitted light pass through a quarter wave plate (retardation angle φ), then followed by a linear polarizer with its transmission axis aligned at an angle θ to the x axis. The emitted light of the single photon source can be decomposed as:

$$E_x(t) = E_{0x}e^{i\delta_x}.e^{i\omega t} = E_x e^{i\omega t} \quad \text{(S18)}$$

$$E_y(t) = E_{0y}e^{i\delta_y}.e^{i\omega t}E_y e^{i\omega t} \quad \text{(S19)}$$

where E_x and E_y are the complex amplitude. The Stokes parameter for a plane wave can be obtained from:

$$\begin{aligned} S_0 &= E_x E_x^* + E_y E_y^* \\ S_1 &= E_x E_x^* - E_y E_y^* \\ S_2 &= E_x E_y^* + E_y E_x^* \\ S_3 &= i(E_x E_x^* + E_y E_y^*) \end{aligned} \quad \text{(S20)}$$

where E_x^* and E_y^* are the complex conjugates of E_x and E_y.

The intensity $I(\varphi, \theta)$ of the emitted light is a function of retardation angle φ and polarizer alignment angle θ:

$$I(\varphi,\theta) = E_x E_x^* \cos^2\theta + E_y E_y^* \sin^2\theta + E_x^* E_y e^{-i\varphi}\sin\theta\cos\theta + E_x E_y^* e^{-i\varphi}\sin\theta\cos\theta \quad \text{(S21)}$$

The intensities at four different pairs of φ and θ are measured to calculate the four Stokes parameter. The first three Stokes parameter is measured by rotating the polarizer to angle $\theta = 0°$, $90°$, $45°$, and $-45°$ respectively (remove the quarter wave plate). The final parameter S_3 is measured by the quarter wave retarder ($\theta = \pm 45°, \varphi = 90°$) and linear polarizer ($\theta = 0°$). The Stokes parameter is derived as:

$$\begin{aligned} S_0 &= I(0°,0°) + I(90°,0°) \\ S_1 &= I(0°,0°) - I(90°,0°) \\ S_2 &= I(45°,0°) - I(-45°,0°) \\ S_3 &= I(45°,90°) - I(-45°,90°) \end{aligned} \quad \text{(S22)}$$

The degree of circular polarization of photon emission is defined as

$$P_c = S_3/\sqrt{(S_1)^2 + (S_2)^2 + (S_3)^2} \quad \text{(S23)}$$

in which S_1, S_2, and S_3 are the Stokes parameters normalized to the corresponding total intensity (S_0) obtained in each measurement.

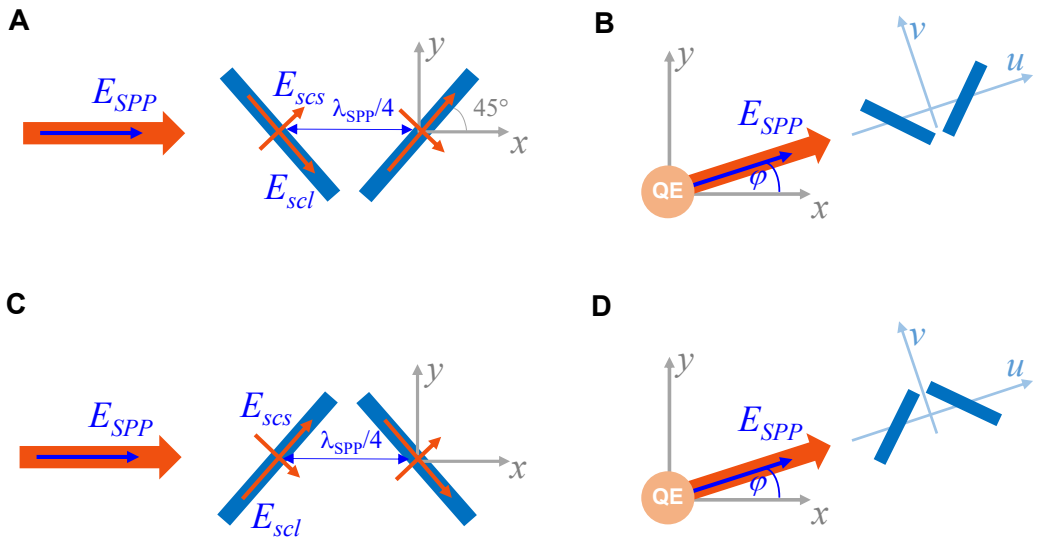

Fig. S1.

Schematic illustration of generating RCP and LCP. (**A, C**) Normal incident SPP scattered by a doublet of anisotropic scatterers. (**B, D)** Regime of QE-excited SPPs propagating under an azimuthal angle φ.

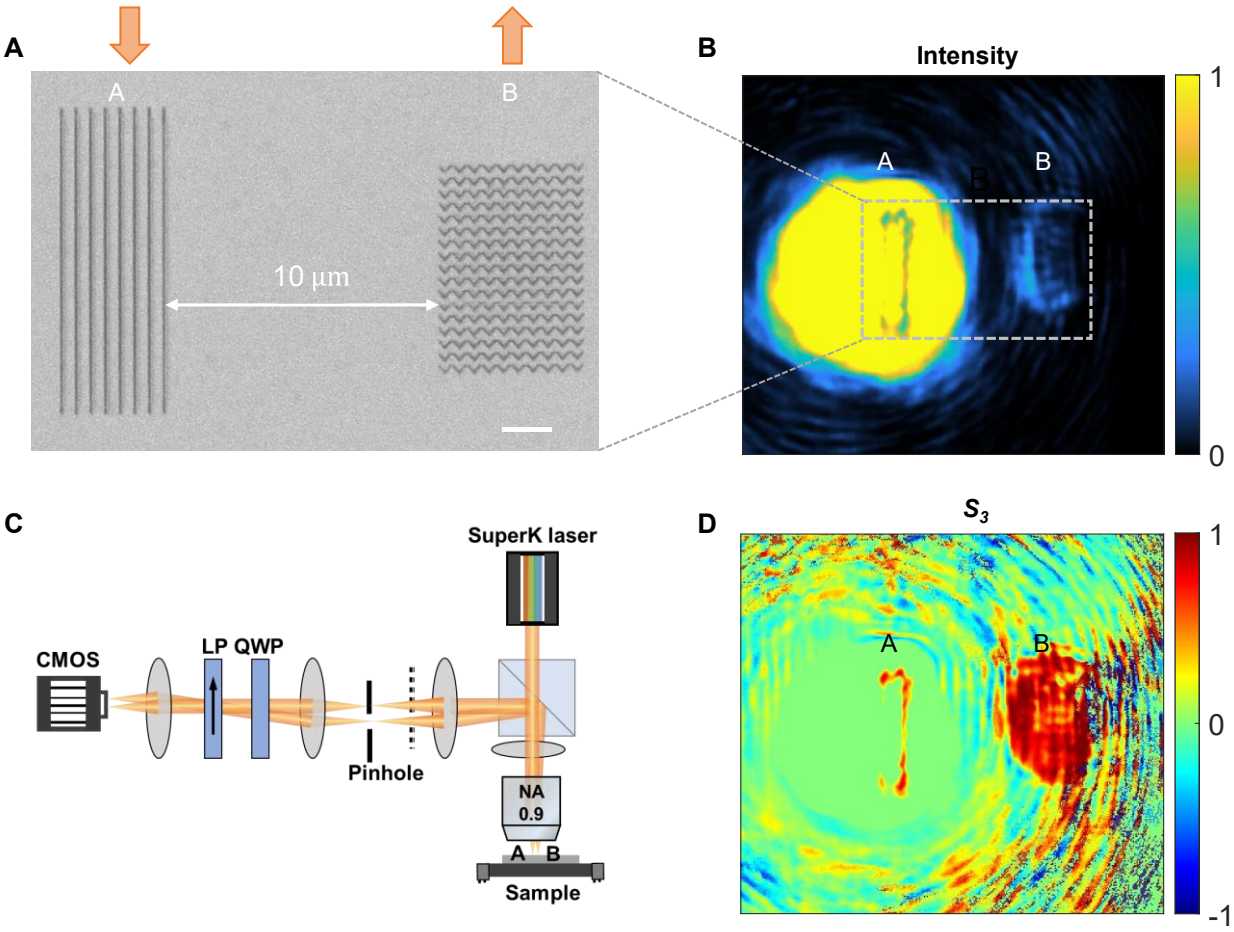

Fig. S2.

Experimental demonstration of RCP generation with optimized element. (**A**) SEM images of the fabricated grating-metasurface. Scale bar: 2 μm. (**B**) The real plane under TM incidence at 670 nm. (**C**) Corresponding experimental setup. (**D**) Measured Stokes parameter S_3.

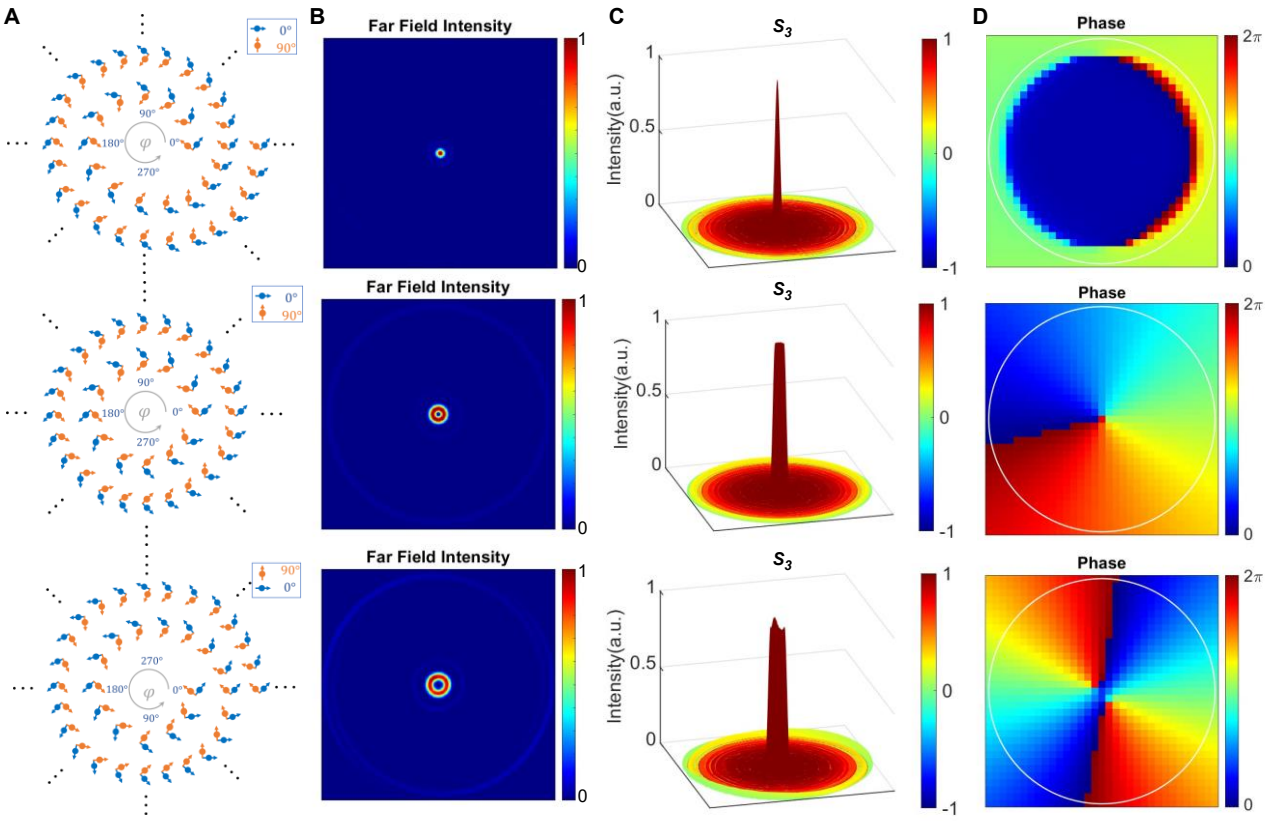

Fig. S3.

Simulated results with dipole arrays, mimicking the designed configuration. (**A**) Schematic of the orthogonal dipole unit arranged with diverging spiral, concentric circle and converging spiral trajectories. There is a phase shift between the orthogonal dipole for each unit, forming perfect circular polarization. (**B**) Far-field angular intensity distribution (in the Fourier plane). (**C**) 3D superimposed intensity and polarization states, the colour shows the Stokes parameter S_3. (**D**) Phase distribution of the decomposed RCP component. The white circle shows the collection angle of NA = 0.1.

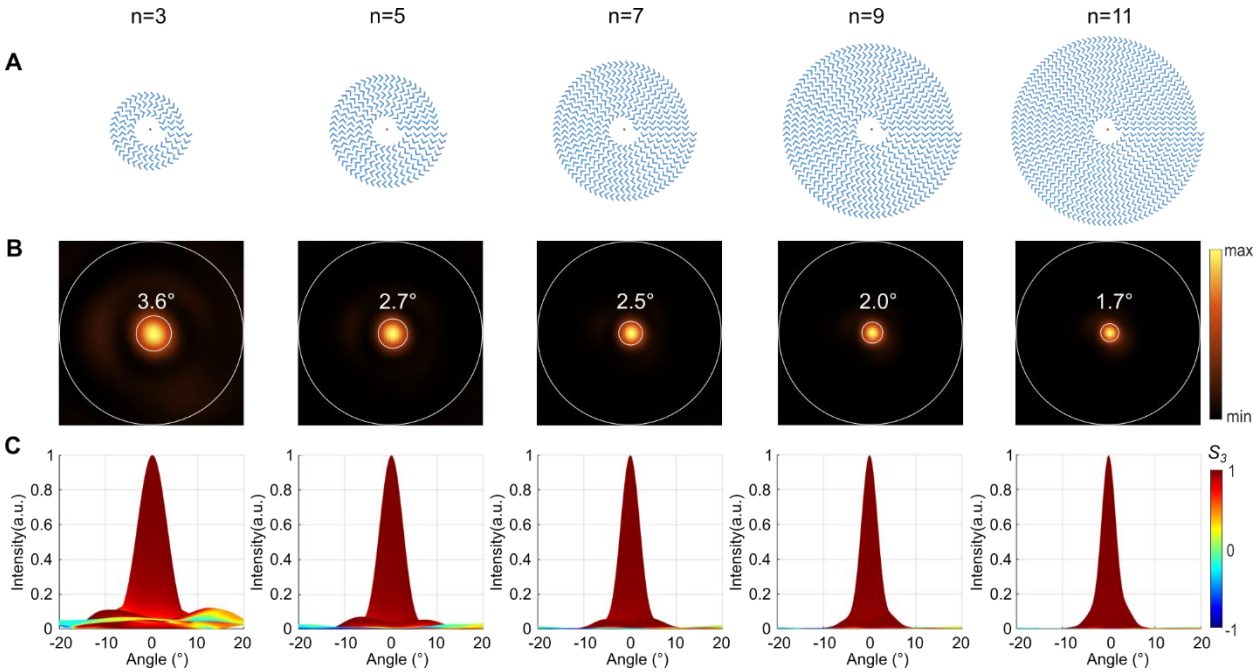

Fig. S4.

Influence of the number of rings on the performance. (**A**) Top view of diverging Archimedean spiral configurations with different number windings (n = 3, 5, 7, 9, and 11). (**B**) Far-field intensity distribution with numerical aperture NA = 0.2. The inner circle denotes the divergence angle. (**C**) The superimposed intensity and degree of circular polarization (the colour represents Stokes parameter S_3).

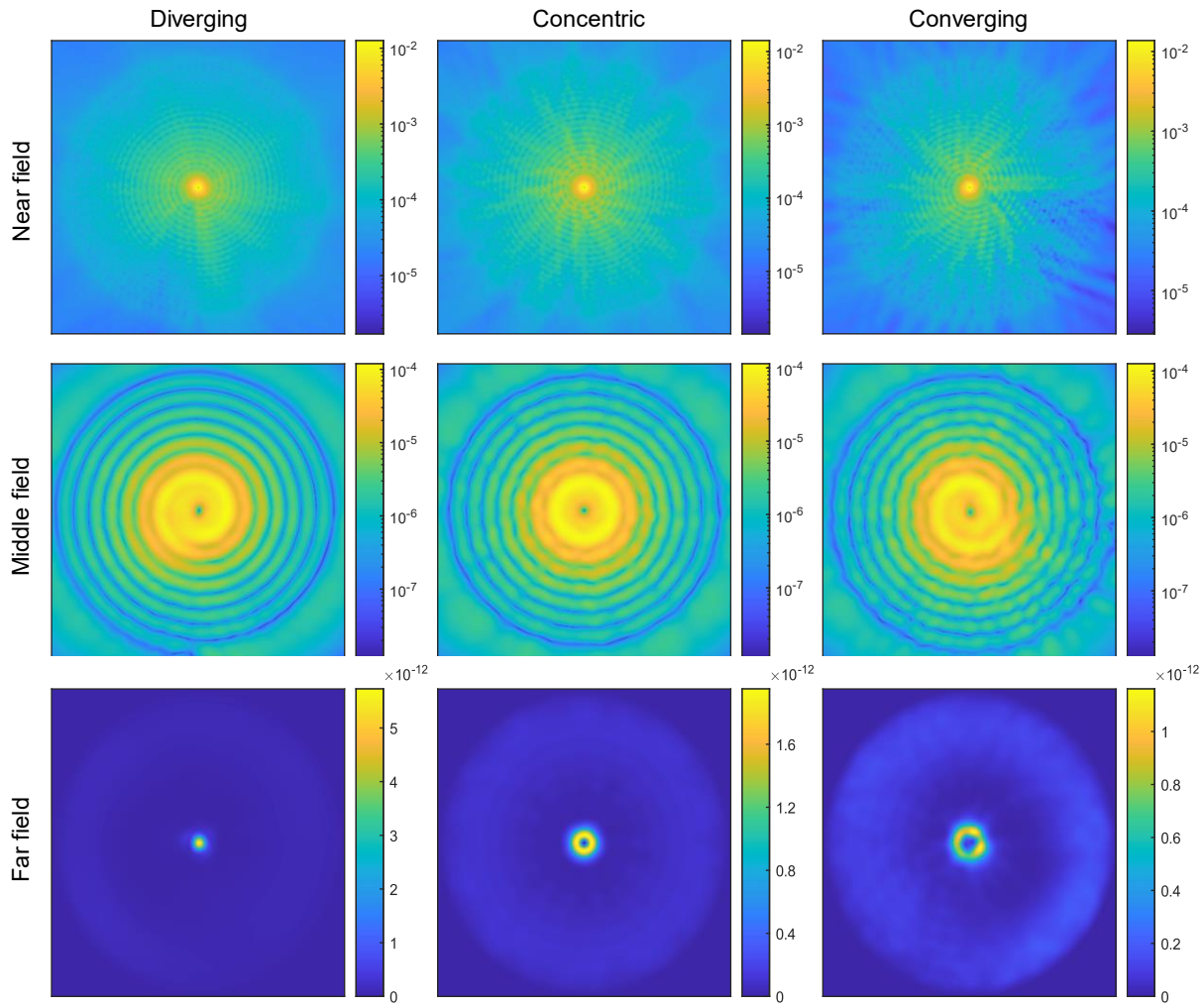

Fig. S5.

Numerical simulations of energy flow (Poynting vector P_z) with designed diverging, concentric, and converging configurations. In the near field, monitor is 30 nm away from metasurface. In the middle field, monitor is 900 nm away from metasurface, the far field is calculated with near to far field transformation. The results present the evolution of energy flow from the dipole source: In the near field, the photon emission is dominated by the dipole source itself; In the middle field, it shows the interactions between the dipole-excited SPPs with the surrounding nanostructures; In the far field, the dipole-excited SPPs are coupled into free space photon emission with different phase profiles (topological charges), showing a bright spot or doughnuts.

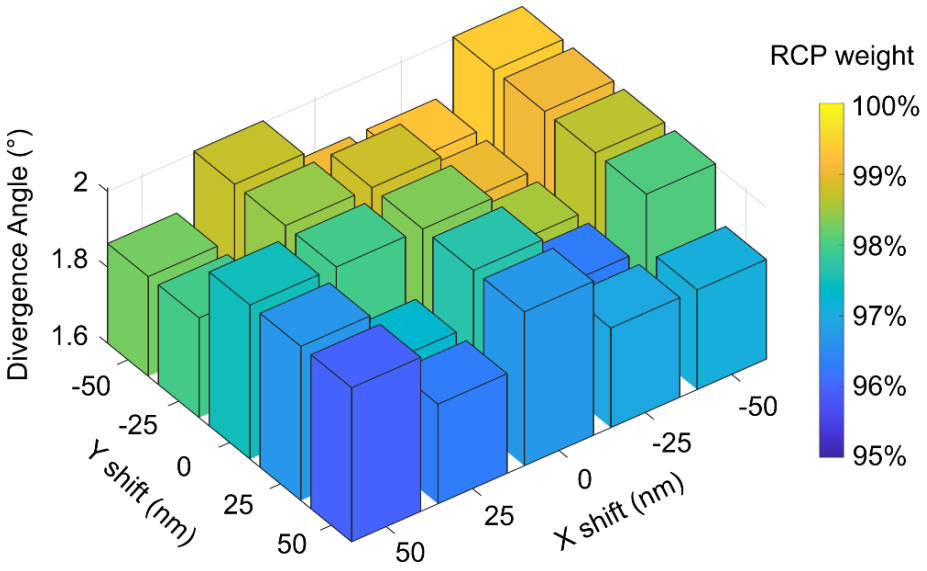

Fig. S6.

Influence of the position shift of QEs on the performance with diverging spiral configuration. The circular polarization purity maintains high value (lager than 95%) and the divergence angle varies from 1.86° to 2°, which are all robust to the position shift of QEs within 50 nm.

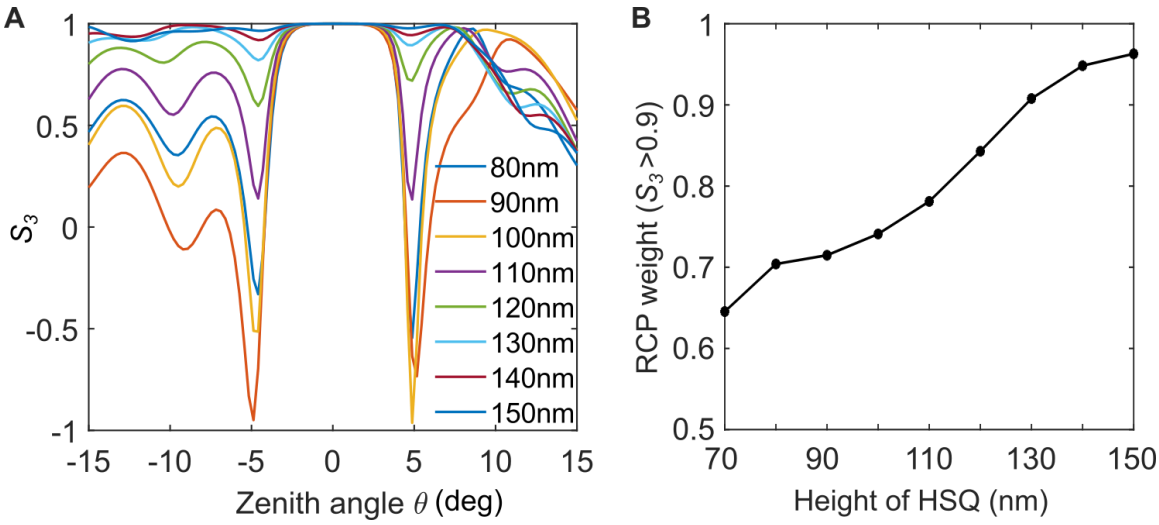

Fig. S7.

Influence of the height of HSQ on the performance of circular polarized states. (**A**) Simulated Stokes parameter S_3 within zenith angle $\pm 15°$. (**B**) Variation of RCP purity with the height of HSQ.

A

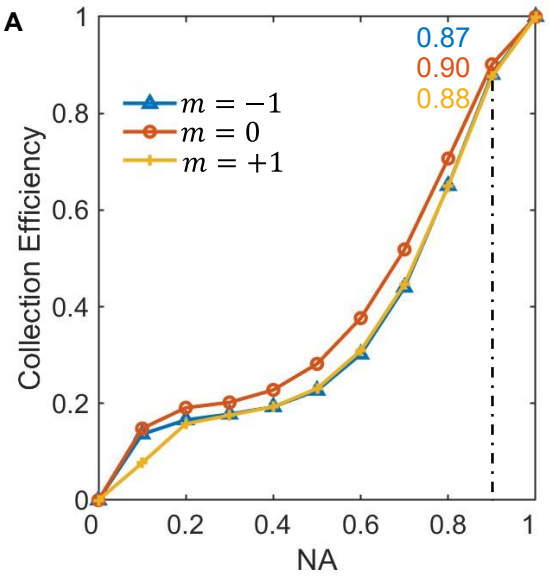

B

Quantum efficiency(TiO_2)	**72.8%**
Quantum efficiency(HSQ)	**32.4%**
Purcell Factor (TiO_2)	**3.53**
Purcell Factor (HSQ)	**3.27**

Fig. S8.

Simulated collection efficiency, quantum efficiency and Purcell factor. (**A**) Collection efficiency as a function of the NA for configurations with diverging spiral ($m = -1$), concentric circle ($m = 0$), and converging spiral ($m = +1$) trajectories. (**B**) Quantum efficiency and Purcell factor with different materials (HSQ and TiO_2) for configuration with diverging spiral ($m = -1$).

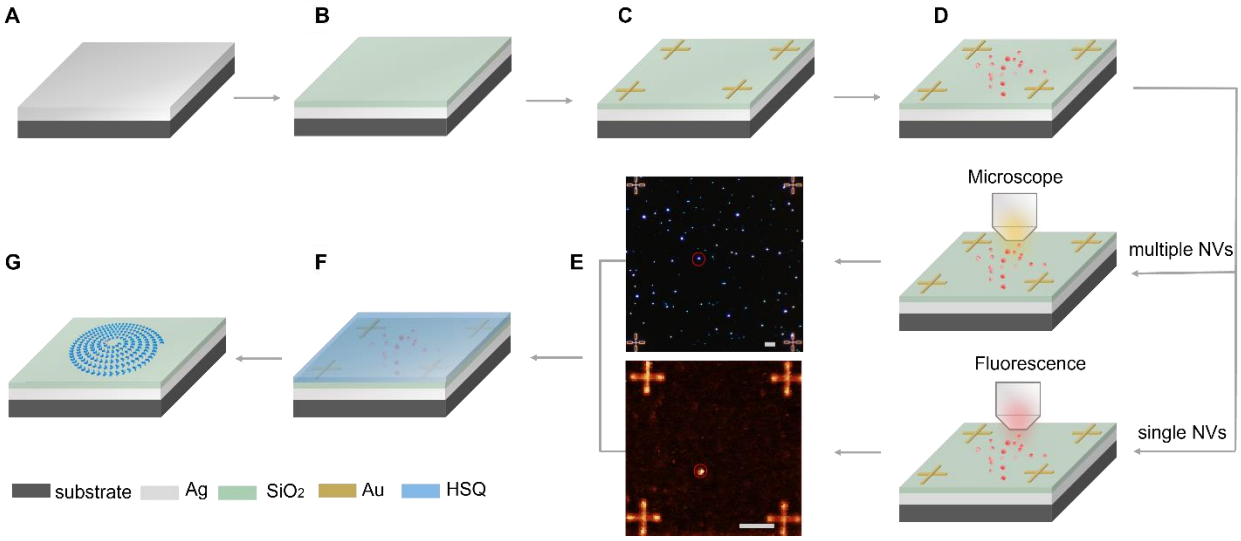

Fig. S9.

Fabrication process of photon sources with multiple ND-NVs and single ND-NV. (**A**) Deposition of 150 nm Ag on the silicon substrate. (**B**) 20 nm SiO_2 deposition. (**C**) The alignment gold markers are fabricated by using EBL, gold deposition, and lift-off process. (**D**) Spin coating nanodiamond containing NVs. (**E**) Determine the position of ND-NVs. A dark-field microscope image is taken to determine the position of ND-NVs. Single-photon ND-NVs is searched by the fluorescence scan with a radially polarized excitation laser beam (532 nm), the position of which is determined by the fluorescence image with the help of alignment markers at the corners of a 27×27 μm^2 area. Scale bar: 5 μm. (**F**) Spin coating HSQ and baked at the hotplate to form 150 nm HSQ layer. (**G**) Metasurfaces are fabricated around the ND-NVs by EBL and the precise alignment procedure. The alignment and position determining method can be found in Ref *(37)*.

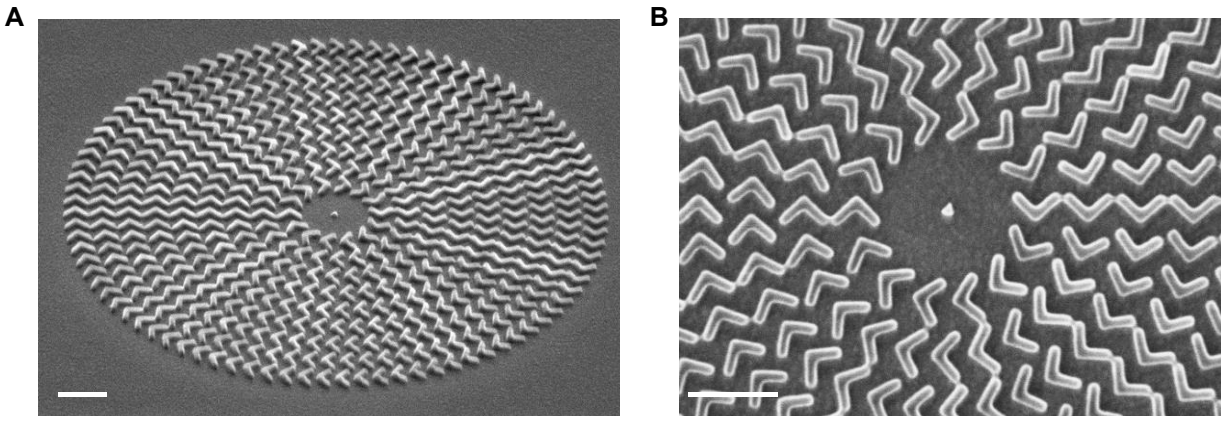

Fig. S10.

SEM of the fabricated devices. (**A**) Angular-view scanning electron micrograph. (**B**) Top-view SEM images of the centre part. ND-NVs is positioned in the center of metasurface. Scale bar: 1 μm.

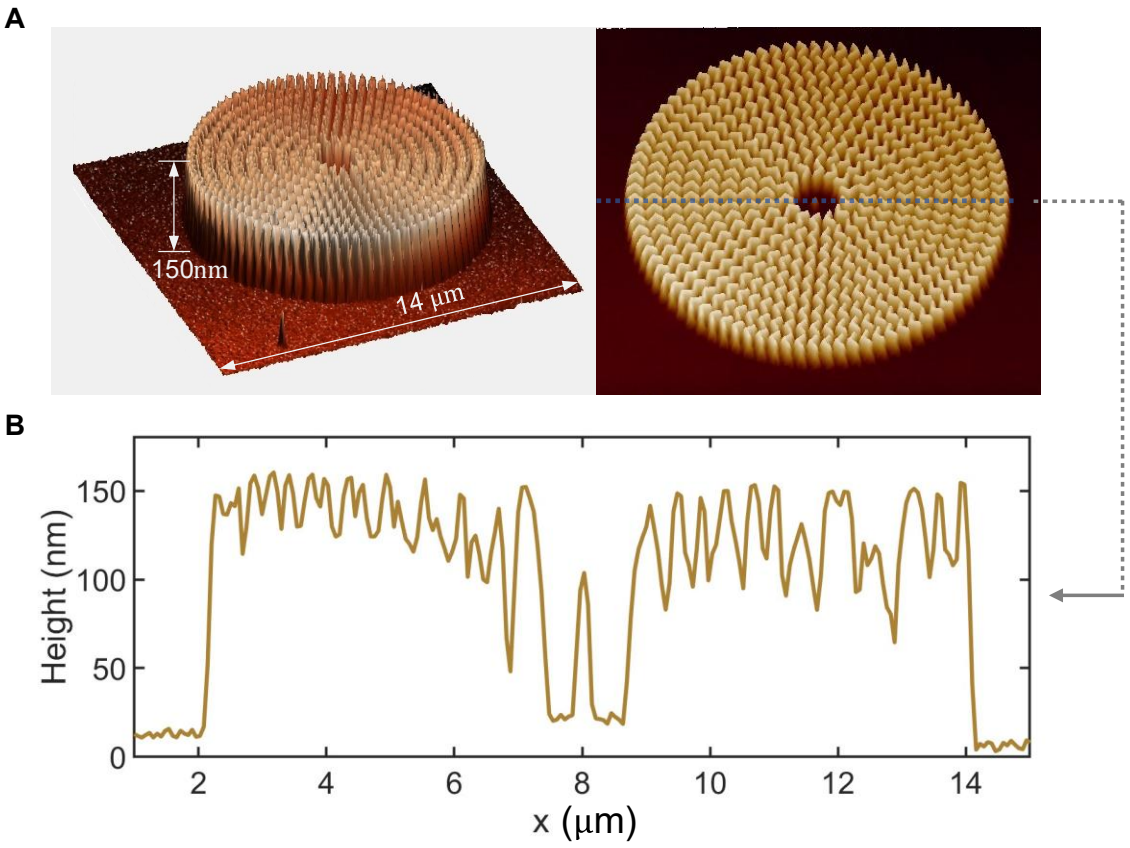

Fig. S11.

AFM of the fabricated devices. (**A**) 3D AFM schematic of the fabricated sample. (**B**) Height of HSQ in the cross section.

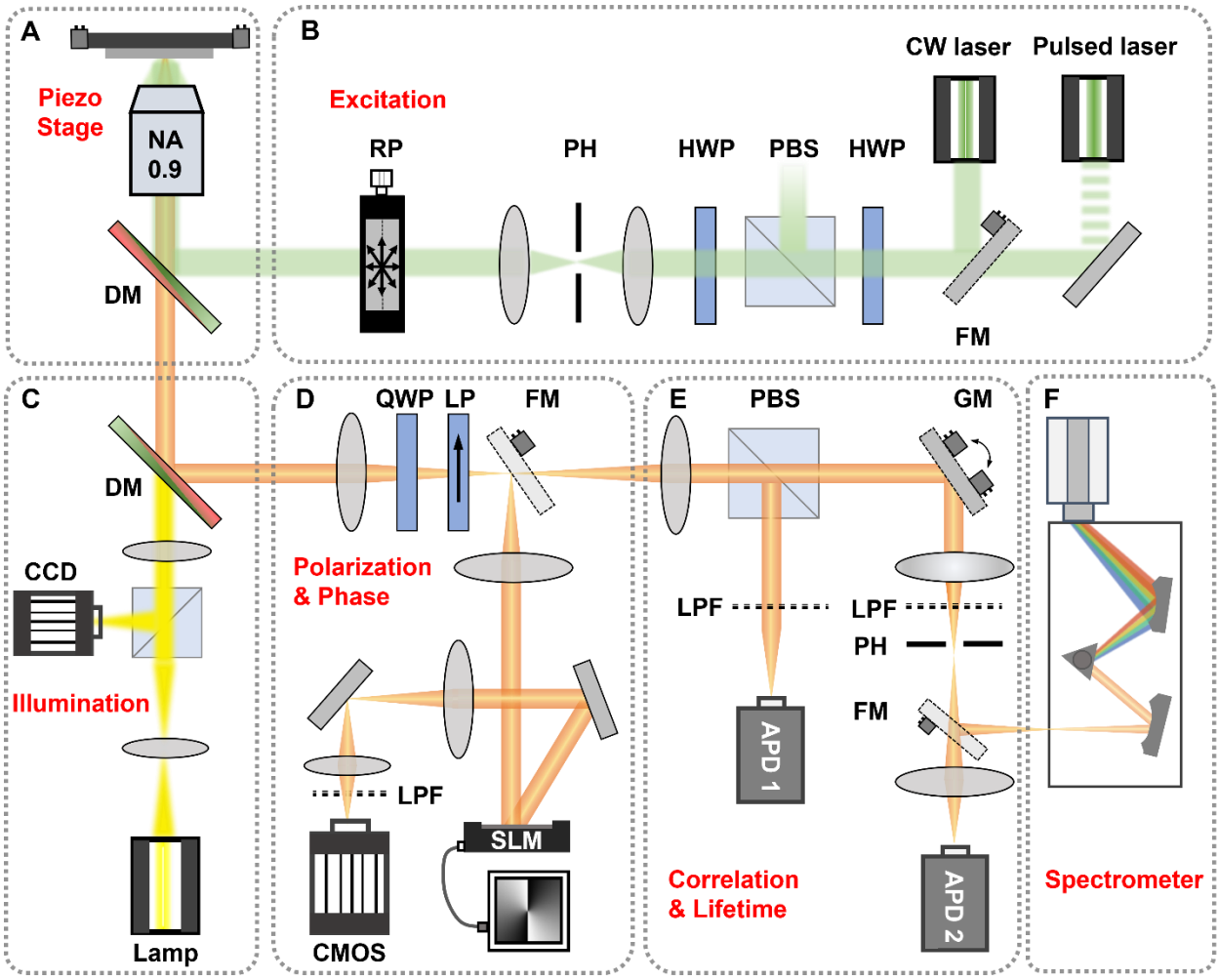

Fig. S12.

Schematic of experimental setup. (**A**) Sample stage. The piezo-stage allows for locating ND-NVs when scanning fluorescence maps. (**B**) Incident light for exciting the nanodiamond. (**C**) Illumination part for finding the fabricated QE-coupled metasurfaces. (**D**) Characterization for polarization states and topological charge. (**E**) Characterization for fluorescence image, correlation, decay-rate. Fluorescence photon rate is recorded by avalanche photo diode (APD1), which is filtered from the laser light, by a set of dichroic mirrors (DM) and a long pass filter (LPF). Correlation measurements is recorded by histogramming the timing delay between photon detection events between APD1 and APD2 in a start-stop configuration, using an electronic timing box (Picharp-300; Pico quant). (**F**) Characterization for spectrum. CW: continuous wave, RP: Radial Polarization Converter, PBS: polarized beam splitter, PH: pinhole, DM: dichroic mirror, LP: linear polarization, QWP: quarter-wave plate, LPF: 550 nm long pass filter, FM: flip mirror, GM: galvanometric mirror. APD: Avalanche Photodiode.

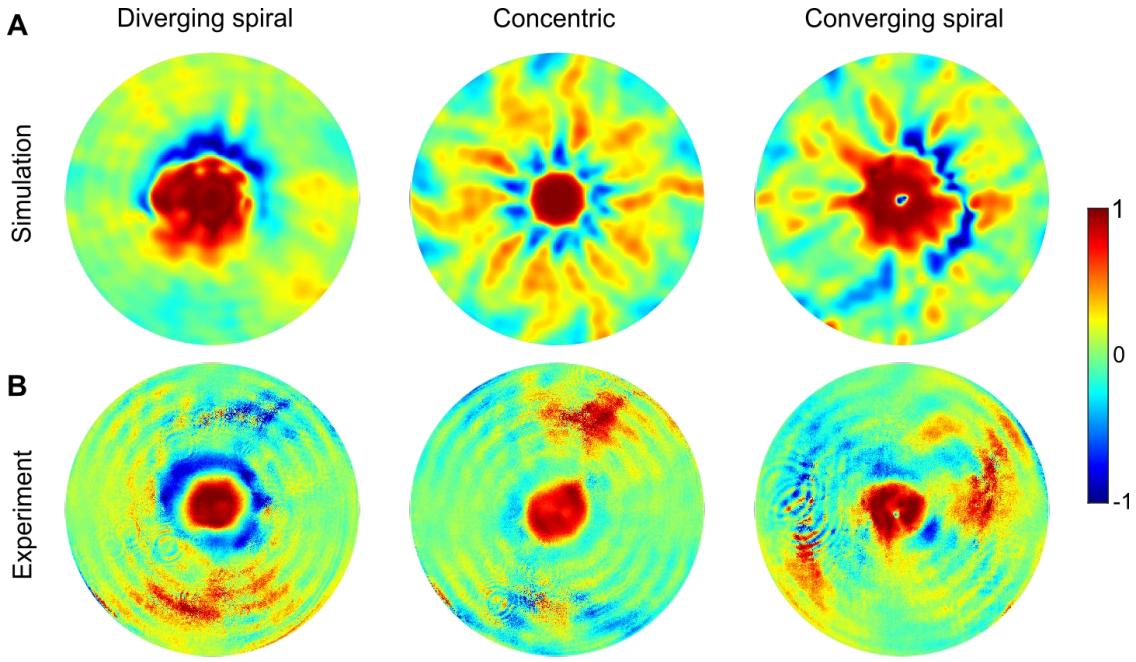

Fig. S13.

Characteristics of the circular polarized states. Simulated (**A**) and measured (**B**) Stokes parameter S_3 distributions of the designed diverging, concentric, and converging configurations.

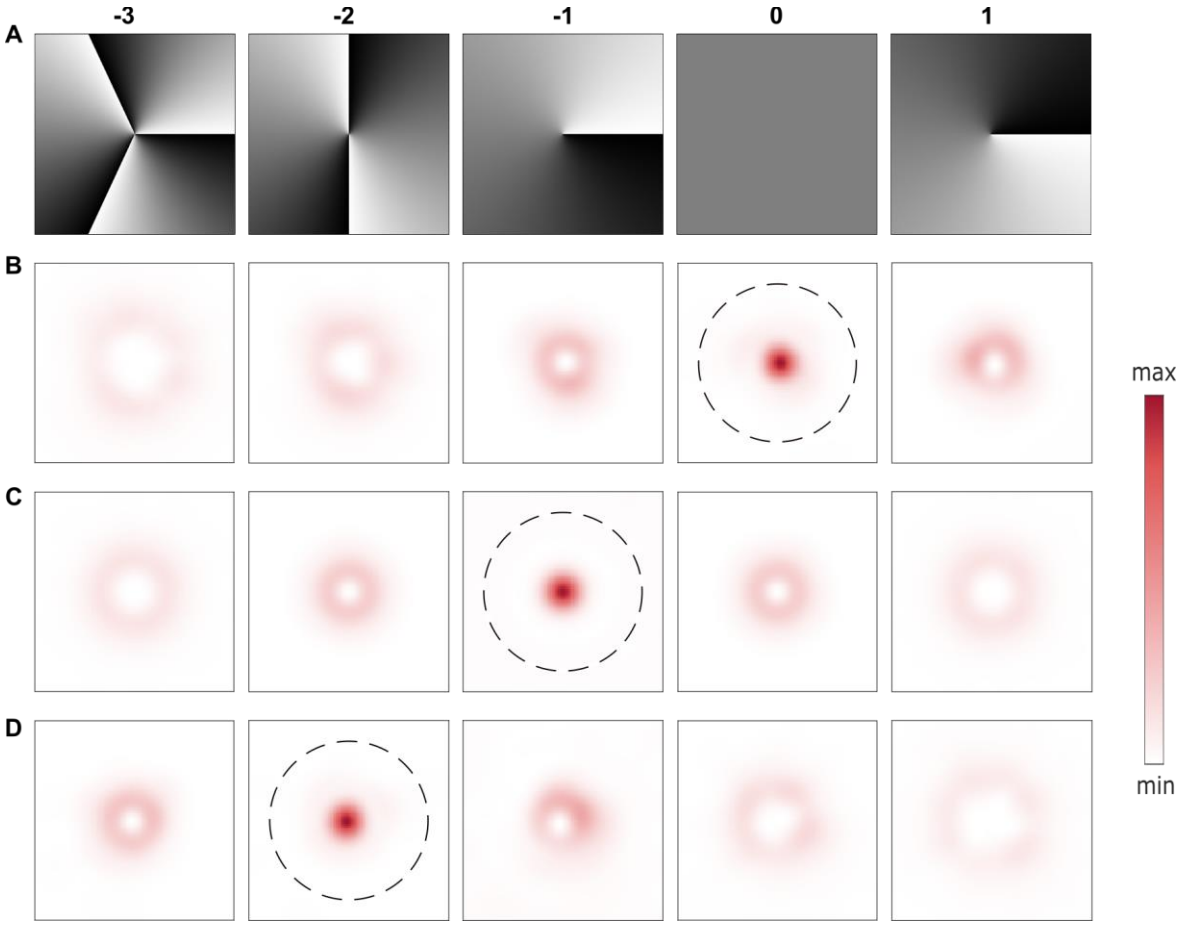

Fig. S14.

Simulated vortex states from QE-couple metasurfaces. (**A**) Phase distribution for holograms with topological charges with -3, -2, -1, 0, and 1. (**B-D**) Simulated intensity distributions of the RCP components of the single-photon emissions that are projected to holograms with (**B**) diverging spiral, (**C**) concentric, (**D**) converging spiral configuration.

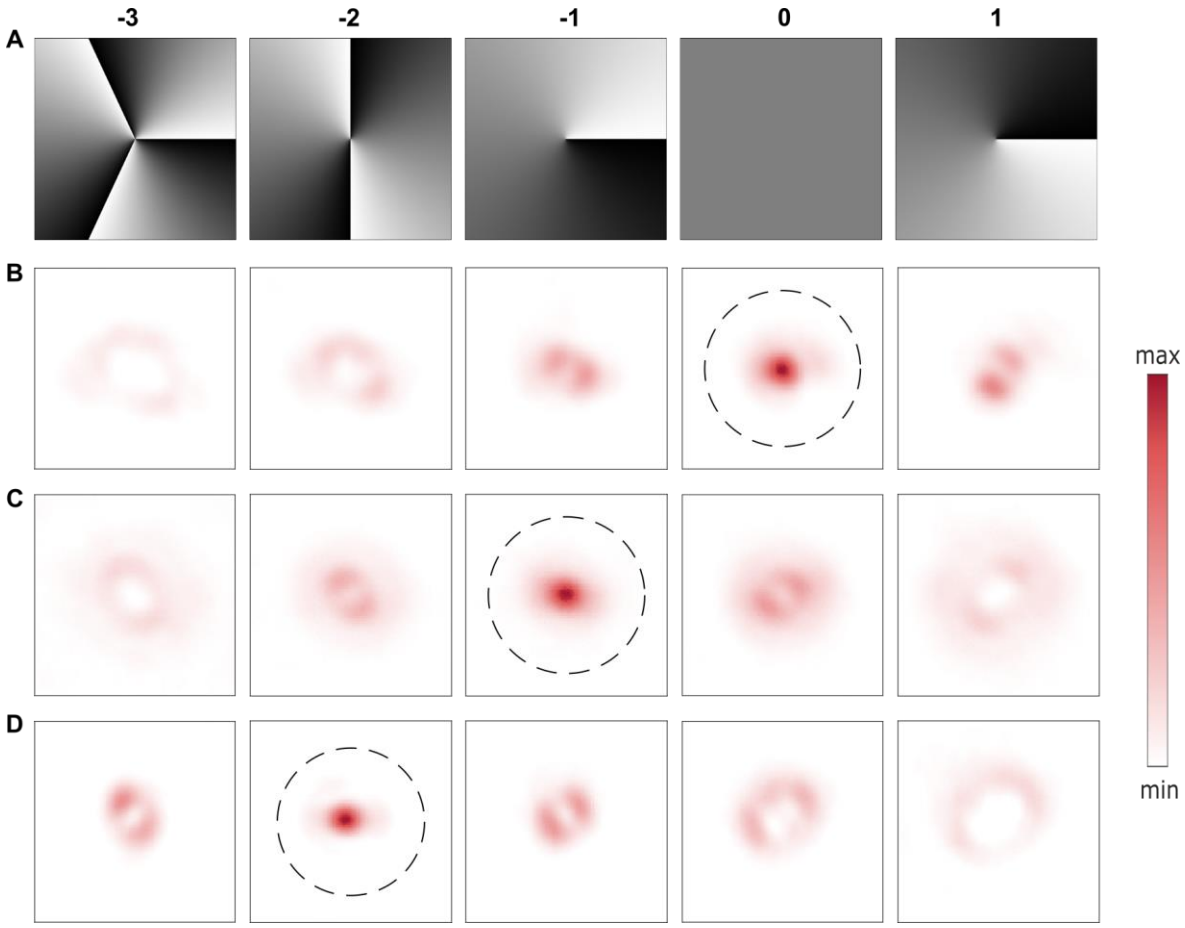

Fig. S15.

Measured vortex states of the designed photon sources with ND-NVs. (**A**) Phase distribution for holograms with topological charges with -3, -2, -1, 0, and 1. (**B-D**) Measured intensity distributions of the RCP components of the single-photon emissions that are projected to holograms with (**B**) diverging spiral, (**C**) concentric, (**D**) converging spiral configuration.

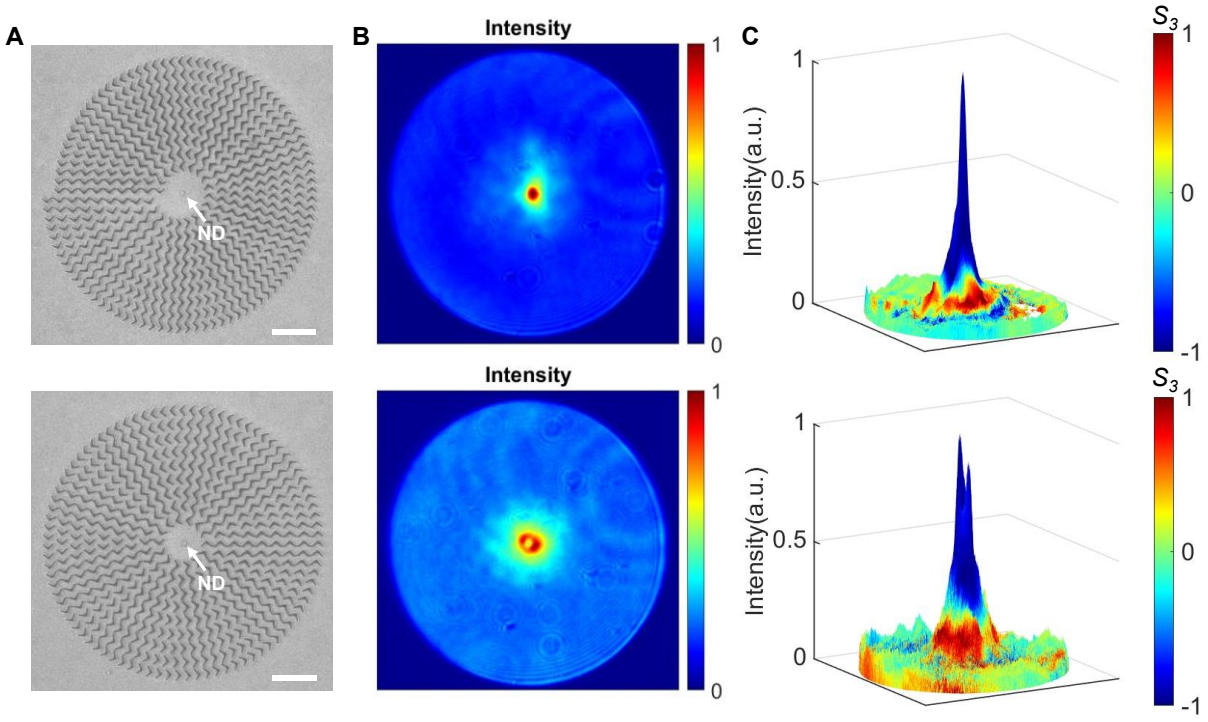

Fig. S16.

Experimental demonstration of left-hand circular polarized (LCP) vortex photon sources. **(A)** SEM images of the fabricated circularly polarized vortex photon sources with topological charge of 0 (top) and 1 (bottom). **(B)** Far-field intensity distribution. **(C)** 3D representation of the superimposed intensity and polarization distribution. The height indicating the intensity and the colour shows the value of Stokes Vector S_3.

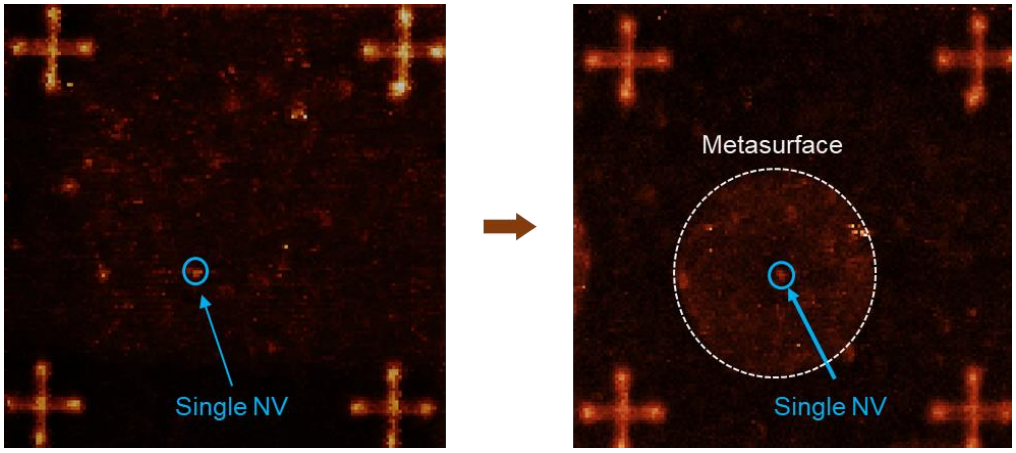

Fig. S17.
Fluorescence image of single-photon source before and after coupling with metasurface.

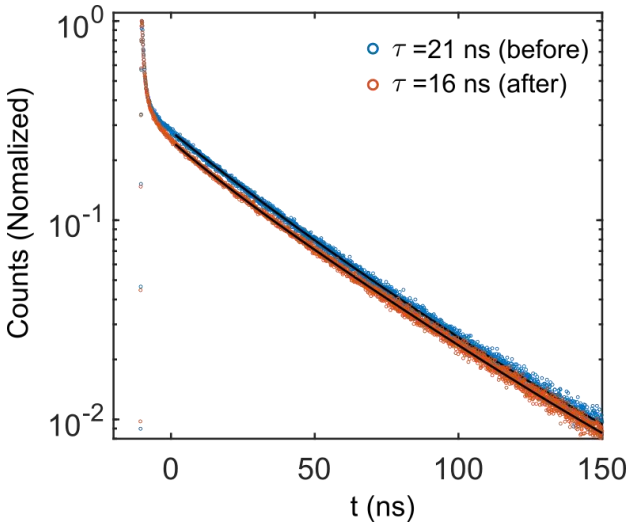

Fig. S18.
Lifetime of single photon sources before and after coupling with metasurfaces.

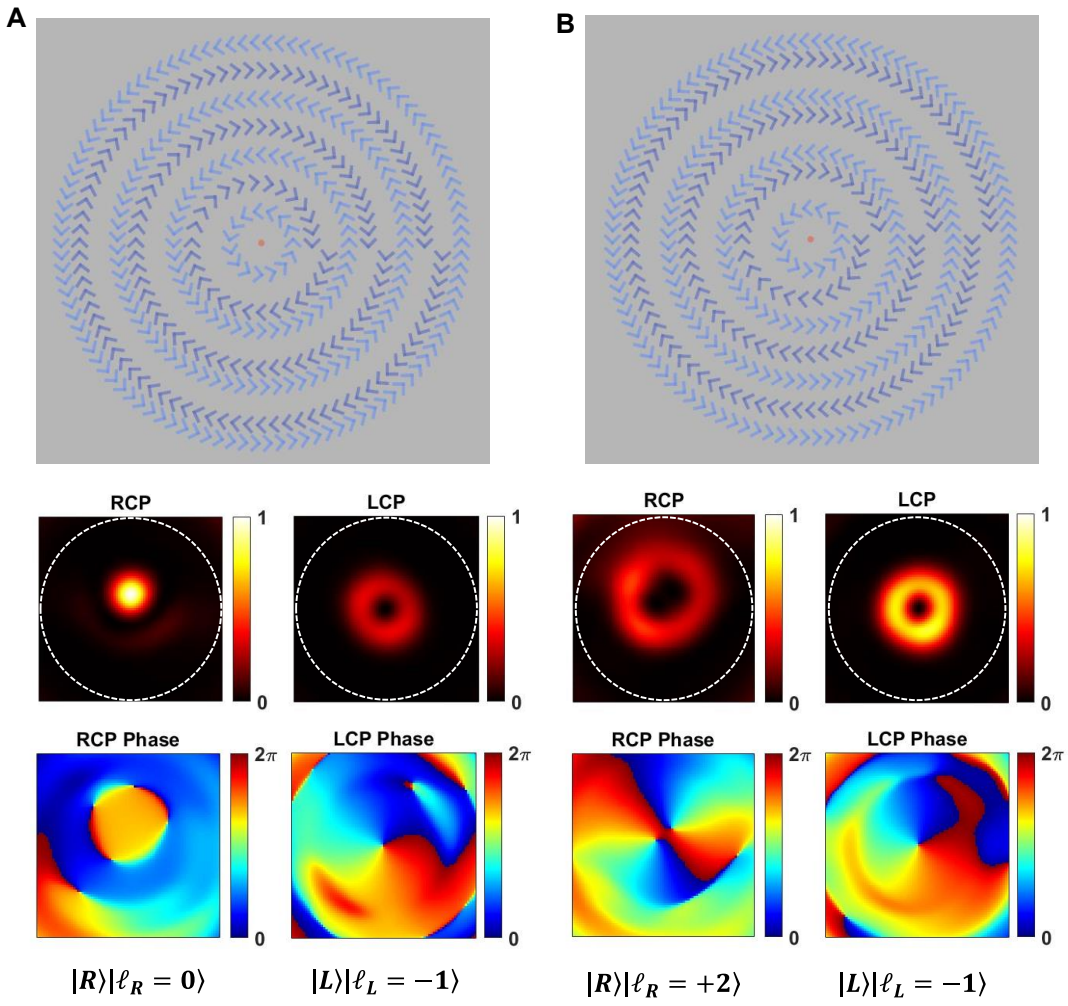

Fig. S19.

Hybrid arrangements of QE-coupled quantum metasurfaces. (**A**) Combination of diverging spiral (RCP element) and concentric (LCP element) for realizing entangled states of $|R\rangle|\ell_R = 0\rangle$ and $|L\rangle|\ell_L = -1\rangle$. (**B**) Combination of converging spiral (RCP element) and concentric (LCP element) for realizing entangled states of $|R\rangle|\ell_R = +2\rangle$ and $|L\rangle|\ell_L = -1\rangle$. The first row is the top view of designed QE-coupled quantum metasurfaces, the second row is the RCP and LCP intensities, the third row is the corresponding phases. Note that all the bricks are made by same dielectric materials (HSQ), the difference of colour in first row just identifies the elements with different orientations that contributes to either RCP or LCP. The white dashed circles denote the numerical aperture NA = 0.2.

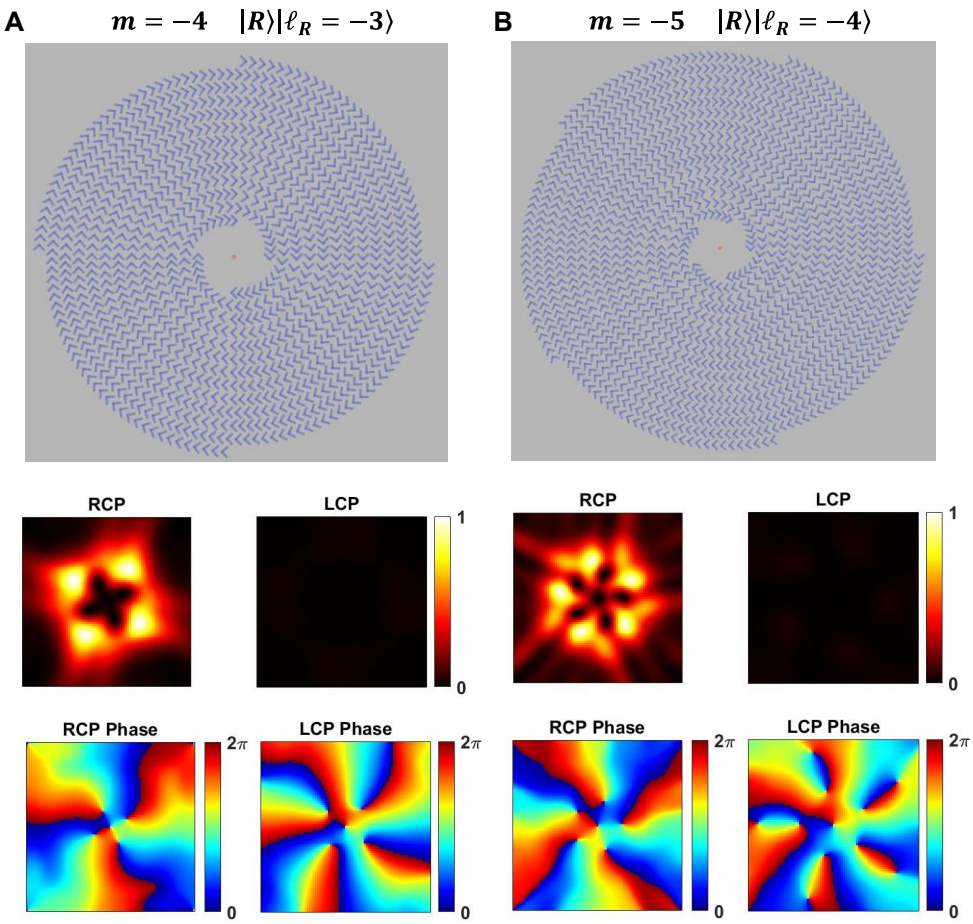

Fig. S20.

High order OAM with different number of spiral arms. (**A**) RCP element arranged with diverging spiral arms ($m = -4$) for realizing states of $|R\rangle|\ell_R = -3\rangle$. (**B**) RCP element arranged with diverging spiral arms ($m = -5$) for realizing states of $|R\rangle|\ell_R = -4\rangle$. m is the number of spiral arms (m < 0 for diverging or m > 0 for converging spirals).

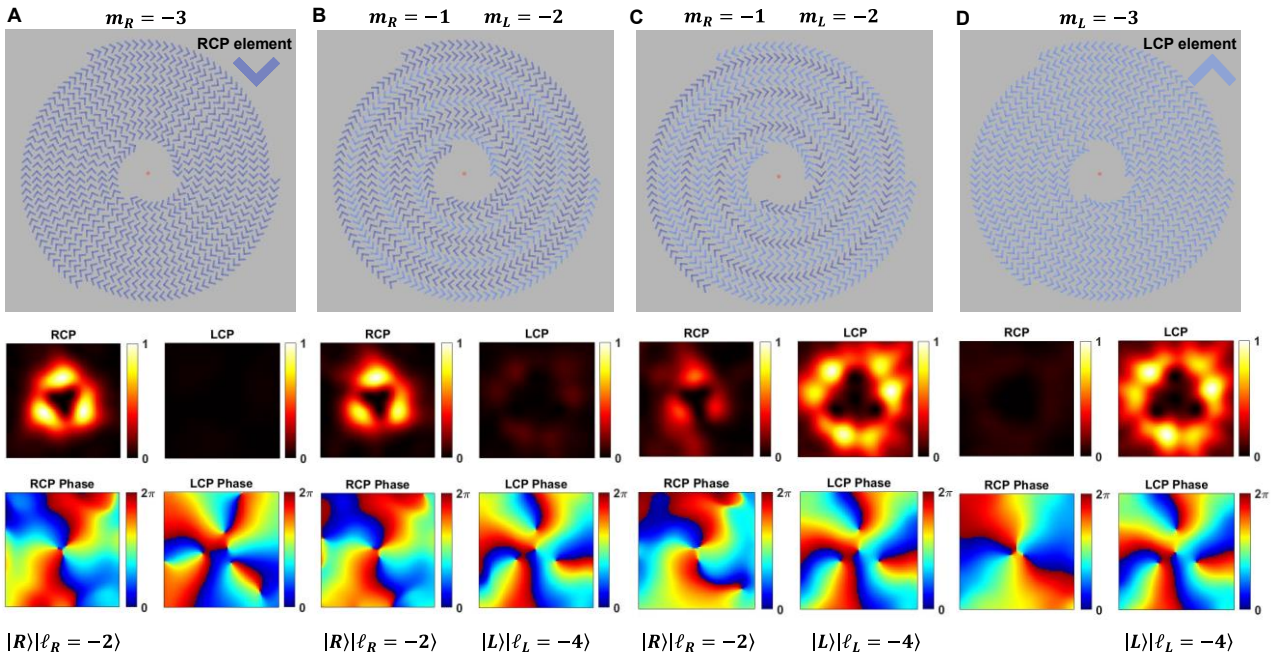

Fig. S21.

Manipulation of SAM and OAM with different chirality of element with a fixed trajectory. (**A**) RCP element arranged with diverging spiral arms ($m = -3$) for realizing states of $|R\rangle|\ell_R = -2\rangle$. (**B**) Combination of RCP element (2 arms) and LCP element (1 arm) for realizing composite states of $|R\rangle|\ell_R = -2\rangle$ and $|L\rangle|\ell_L = -4\rangle$, dominated by $|R\rangle|\ell_R = -2\rangle$. (**C**) Combination of RCP element (1 arm) and LCP element (2 arms) for realizing states of $|R\rangle|\ell_R = -2\rangle$ and $|L\rangle|\ell_L = -4\rangle$, dominated by $|L\rangle|\ell_L = -4\rangle$. (**D**) LCP element arranged with diverging spiral arms ($m = -3$) for realizing states of $|L\rangle|\ell_L = -4\rangle$.

REFERENCES AND NOTES

1. A. Mair, A. Vaziri, G. Weihs, A. Zeilinger, Entanglement of the orbital angular momentum states of photons. *Nature* **412**, 313–316 (2001).

2. G. Molina-Terriza, J. P. Torres, L. Torner, Twisted photons. *Nat. Phys.* **3**, 305 (2007), 310.

3. C. H. Bennett, D. P. DiVincenzo, Quantum information and computation. *Nature* **404**, 247–255 (2000).

4. N. Gisin, R. Thew, Quantum communication. *Nat. Photon.* **1**, 165–171 (2007).

5. X.-L. Wang, X.-D. Cai, Z.-E. Su, M.-C. Chen, D. Wu, L. Li, N.-L. Liu, C.-Y. Lu, J.-W. Pan, Quantum teleportation of multiple degrees of freedom of a single photon. *Nature* **518**, 516–519 (2015).

6. A. Sit, F. Bouchard, R. Fickler, J. Gagnon-Bischoff, H. Larocque, K. Heshami, D. Elser, C. Peuntinger, K. Günthner, B. Heim, C. Marquardt, G. Leuchs, R. W. Boyd, E. Karimi, High-dimensional intracity quantum cryptography with structured photons. *Optica* **4**, 1006–1010 (2017).

7. A. Fleischer, O. Kfir, T. Diskin, P. Sidorenko, O. Cohen, Spin angular momentum and tunable polarization in high-harmonic generation. *Nat. Photonics* **8**, 543–549 (2014).

8. P. Lodahl, S. Mahmoodian, S. Stobbe, A. Rauschenbeutel, P. Schneeweiss, J. Volz, H. Pichler, P. Zoller, Chiral quantum optics. *Nature* **541**, 473–480 (2017).

9. A. Javadi, D. Ding, M. H. Appel, S. Mahmoodian, M. C. Löbl, I. Söllner, R. Schott, C. Papon, T. Pregnolato, S. Stobbe, L. Midolo, T. Schröder, A. D. Wieck, A. Ludwig, R. J. Warburton, P. Lodahl, Spin–photon interface and spin-controlled photon switching in a nanobeam waveguide. *Nat. Nanotechnol.* **13**, 398–403 (2018).

10. J. Wang, J.-Y. Yang, I. M. Fazal, N. Ahmed, Y. Yan, H. Huang, Y. Ren, Y. Yue, S. Dolinar, M. Tur, A. E. Willner, Terabit free-space data transmission employing orbital angular momentum multiplexing. *Nat. Photon.* **6**, 488–496 (2012).

11. N. Bozinovic, Y. Yue, Y. Ren, M. Tur, P. Kristensen, H. Huang, A. E. Willner, S. Ramachandran, Terabit-scale orbital angular momentum mode division multiplexing in fibers. *Science* **340**, 1545–1548 (2013).

12. Z.-Y. Zhou, Y. Li, D.-S. Ding, W. Zhang, S. Shi, B.-S. Shi, G.-C. Guo, Orbital angular momentum photonic quantum interface. *Light Sci. Appl* **5**, e16019 (2016).

13. H. H. Arnaut, G. A. Barbosa, Orbital and intrinsic angular momentum of single photons and entangled pairs of photons generated by parametric down-conversion. *Phys. Rev. Lett.* **85**, 286–289 (2000).

14. X. Chen, X. Lu, S. Dubey, Q. Yao, S. Liu, X. Wang, Q. Xiong, L. Zhang, A. Srivastava, Entanglement of single-photons and chiral phonons in atomically thin WSe_2. *Nat. Phys.* **15**, 221–227 (2019).

15. S. Liu, Y. Lou, J. Jing, Orbital angular momentum multiplexed deterministic all-optical quantum teleportation. *Nat. Commun.* **11**, 3875 (2020).

16. G. Li, A. S. Sheremet, R. Ge, T. C. H. Liew, A. V. Kavokin, Design for a nanoscale single-photon spin splitter for modes with orbital angular momentum. *Phys. Rev. Lett.* **121**, 053901 (2018).

17. D. Braukmann, E. R. Glaser, T. A. Kennedy, M. Bayer, J. Debus, Circularly polarized zero-phonon transitions of vacancies in diamond at high magnetic fields. *Phys. Rev. B* **97**, 195448 (2018).

18. I. Söllner, S. Mahmoodian, S. L. Hansen, L. Midolo, A. Javadi, G. Kiršanskė, T. Pregnolato, H. El-Ella, E. H. Lee, J. D. Song, S. Stobbe, P. Lodahl, Deterministic photon–emitter coupling in chiral photonic circuits. *Nat. Nanotechnol.* **10**, 775–778 (2015).

19. B. Chen, Y. Wei, T. Zhao, S. Liu, R. Su, B. Yao, Y. Yu, J. Liu, X. Wang, Bright solid-state sources for single photons with orbital angular momentum. *Nat. Nanotechnol.* **16**, 302–307 (2021).

20. Y. Ma, H. Zhao, N. Liu, Z. Gao, S. S. Mohajerani, L. Xiao, J. Hone, L. Feng, S. Strauf, On-chip spin-orbit locking of quantum emitters in 2D materials for chiral emission. *Optica* **9**, 953–958 (2022).

21. P. G. Kwiat, K. Mattle, H. Weinfurter, A. Zeilinger, A. V. Sergienko, Y. Shih, New high-intensity source of polarization-entangled photon pairs. *Phys. Rev. Lett.* **75**, 4337–4341 (1995).

22. T. Santia-Cruz, S. D. Gennaro, O. Mitrofanov, S. Addamane, J. Reno, I. Brener, M. V. Chekhova, Resonant metasurfaces for generating complex quantum states. *Science*, **377**, 991–995 (2022).

23. T. Stav, A. Faerman, E. Maguid, D. Oren, V. Kleiner, E. Hasman, M. Segev, Quantum entanglement of the spin and orbital angular momentum of photons using metamaterials. *Science* **361**, 1101–1104 (2018).

24. K. Wang, J. G. Titchener, S. S. Kruk, L. Xu, H.-P. Chung, M. Parry, I. I. Kravchenko, Y.-H. Chen, A. S. Solntsev, Y. S. Kivshar, D. N. Neshev, A. A. Sukhorukov, Quantum metasurface for multiphoton interference and state reconstruction. *Science* **361**, 1104–1108 (2018).

25. W. J. M. Kort-Kamp, A. K. Azad, D. A. R. Dalvit, Space-time quantum metasurfaces. *Phys. Rev. Lett.* **127**, 043603 (2021).

26. N. Yu, F. Capasso, Flat optics with designer metasurfaces. *Nat. Mater.* **13**, 139–150 (2014).

27. N. Meinzer, W. L. Barnes, I. R. Hooper, Plasmonic meta-atoms and metasurfaces. *Nat. Photon.* **8**, 889–898 (2014).

28. A. V. Kildishev, A. Boltasseva, V. M. Shalaev, Planar photonics with metasurfaces. *Science* **339**, 1232009 (2013).

29. C.-W. Qiu, T. Zhang, G. Hu, Y. Kivshar, Quo Vadis, metasurfaces? *Nano Lett.* **21**, 5461–5474 (2021).

30. Y. Ming, Y. Intaravanne, H. Ahmed, M. Kenney, Y. Lu, X. Chen, Creating composite vortex beams with a single geometric metasurface. *Adv.Mater.* **34**, 2109714 (2022).

31. A.H. Dorrah, F. Capasso, Tunable structured light with flat optics. *Science* **376**, eabi6860 (2022).

32. A. S. Solntsev, G. S. Agarwal, Y. S. Kivshar, Metasurfaces for quantum photonics. *Nat. Photonics* **15**, 327–336 (2021).

33. Y. Kan, F. Ding, C. Zhao, S. I. Bozhevolnyi, Directional off-normal photon streaming from hybrid plasmon-emitter coupled metasurfaces. *ACS Photonics* **7**, 1111–1116 (2020).

34. R. Bekenstein, I. Pikovski, H. Pichler, E. Shahmoon, S. F. Yelin, M. D. Lukin, Quantum metasurfaces with atom arrays. *Nat. Phys.* **16**, 676–681 (2020).

35. Y. Kan, S. I. Bozhevolnyi, Molding photon emission with hybrid plasmon-emitter coupled metasurfaces. *Adv. Optical Mater.* **10**, 2102697 (2022).

36. L. Li, Z. Liu, X. Ren, S. Wang, V. C. Su, M. K. Chen, C. H. Chu, H. Y. Kuo, B. Liu, W. Zang, G. Guo, L. Zhang, Z. Wang, S. Zhu, D. P. Tsai, Metalens-array–based high-dimensional and multiphoton quantum source. *Science* **368**, 1487–1490 (2020).

37. Y. Kan, S. K. H. Andersen, F. Ding, S. Kumar, C. Zhao, S. I. Bozhevolnyi, Metasurface-enabled generation of circularly polarized single photons. *Adv. Mater.* **32**, 1907832 (2020).

38. D. Komisar, S. Kumar, Y. Kan, C. Wu, S. I. Bozhevolnyi, Generation of radially polarized single photons with plasmonic bullseye antennas. *ACS Photonics* **8**, 2190–2196 (2021).

39. C. Wu, S. Kumar, Y. Kan, D. Komisar, Z. Wang, S. I. Bozhevolnyi, F. Ding, Room-temperature on-chip orbital angular momentum single-photon sources. *Sci. Adv.* **8**, eabk3075 (2022).

40. J. Ni, C. Huang, L.-M. Zhou, M. Gu, Q. Song, Y. Kivshar, C.-W. Qiu, Multidimensional phase singularities in nanophotonics. *Science* **374**, eabj0039 (2021).

41. A. Pors, M. G. Nielsen, G. D. Valle, M. Willatzen, O. Albrektsen, S. I. Bozhevolnyi, Plasmonic metamaterial wave retarders in reflection by orthogonally oriented detuned electrical dipoles. *Opt. Lett.* **36**, 1626–1628 (2011).

42. A. Pors, S. I. Bozhevolnyi, Efficient and broadband quarter-wave plates by gap-plasmon resonators. *Opt. Express* **21**, 2942–2952 (2013).

43. S. Kumar, C. Wu, D. Komisar, Y. Kan, L. F. Kulikova, V. A. Davydov, V. N. Agafonov, S. I. Bozhevolnyi, Fluorescence enhancement of a single germanium vacancy center in a nanodiamond by a plasmonic Bragg cavity. *J. Chem. Phys.* **154**, 044303 (2021).

44. A. Forbes, M. De Oliveira, M. R. Dennis, Structured light. *Nat. Photonics* **15**, 253–262 (2021).

45. J. Zhu, Y. Chen, Y. Zhang, X. Cai, S. Yu, Spin and orbital angular momentum and their conversion in cylindrical vector vortices. *Opt. Lett.* **39**, 4435–4438 (2014).

46. H. G. Berry, G. Gabrielse, A. E. Livingston, Measurement of the Stokes parameters of light. *Appl. Optics* **16**, 3200–3205 (1977).

47. S. K. H. Andersen, S. Bogdanov, O. Makarova, Y. Xuan, M. Y. Shalaginov, A. Boltasseva, S. I. Bozhevolnyi, V. M. Shalaev, Hybrid plasmonic bullseye antennas for efficient photon collection. *ACS Photonics* **5**, 692–698, (2018).

48. H. Wang, Y. M. He, T. H. Chung, H. Hu, Y. Yu, S. Chen, X. Ding, M. C. Chen, J. Qin, X. Yang, R. Z. Liu, Z. C. Duan, J. P. Li, S. Gerhardt, K. Winkler, J. Jurkat, L. J. Wang, N. Gregersen, Y. H. Huo, Q. Dai, S. Yu, S. Höfling, C. Y. Lu, J. W. Pan, Towards optimal single-photon sources from polarized microcavities. *Nat. Photonics* **13**, 770–775 (2019).

49. J. Liu, R. Su, Y. Wei, B. Yao, S. F. C. da Silva, Y. Yu, J. Iles-Smith, K. Srinivasan, A. Rastelli, J. Li, X. Wang, A solid-state source of strongly entangled photon pairs with high brightness and indistinguishability. *Nat. Nanotechnol.* **14**, 586–593 (2019).

50. H. Wang, H. Hu, T. H. Chung, J. Qin, X. Yang, J. P. Li, R. Z. Liu, H. S. Zhong, Y. M. He, X. Ding, Y. H. Deng, Q. Dai, Y. H. Huo, S. Höfling, C. Y. Lu, J. W. Pan, On-demand semiconductor source of entangled photons which simultaneously has high fidelity, efficiency, and indistinguishability. *Phys. Rev. Lett.* **122**, 113602 (2019).

51. A. Pors, M. G. Nielsen, S. I. Bozhevolnyi, Plasmonic metagratings for simultaneous determination of Stokes parameters. *Optica* **2**, 716–723, (2015).

52. A. Yariv, P. Yeh, *Optical Waves in Crystals* (Wiley, 1984), vol. 5.